Large Tolerance of Lasing Properties to Impurity Defects in GaAs(Sb)-AlGaAs Core-Shell Nanowire Lasers

Tobias Schreitmüller, Hyowon W. Jeong, Hamidreza Esmaielpour, Christopher E. Mead, Manfred Ramsteiner, Paul Schmiedeke, Andreas Thurn, Akhil Ajay, Sonja Matich, Markus Döblinger, Lincoln J. Lauhon, Jonathan J. Finley, and Gregor Koblmüller*

GaAs-AlGaAs based nanowire (NW) lasers hold great potential for on-chip photonic applications, where lasing metrics have steadily improved over the years by optimizing resonator design and surface passivation methods. The factor that will ultimately limit the performance will depend on material properties, such as native- or impurity-induced point defects and their impact on non-radiative recombination. Here, the role of impurity-induced point defects on the lasing performance of low-threshold GaAs(Sb)-AlGaAs NW-lasers is evaluated, particularly by exploring Si-dopants and their associated vacancy complexes. Si-induced point defects and their self-compensating nature are identified using correlated atom probe tomography, resonant Raman scattering, and photoluminescence experiments. Under pulsed optical excitation the lasing threshold is remarkably low (<10 µJ cm^{-2}) and insensitive to impurity defects over a wide range of Si doping densities, while excess doping ([Si]$>10^{19}$ cm^{-3}) imposes increased threshold at low temperature. These characteristics coincide with increased Shockley-Read-Hall recombination, reflected by shorter carrier lifetimes, and reduced internal quantum efficiencies (IQE) . Remarkably, despite the lower IQE the presence of self-compensating Si-vacancy defects provides an improved temperature stability in lasing threshold with higher characteristic temperature and room-temperature lasing. These findings highlight an overall large tolerance of lasing metrics to impurity defects in GaAs-AlGaAs based NW-lasers.

1. Introduction

The quest for ultracompact, on-chip coherent light sources increasingly aims at new high-performance materials and down-scaled device geometries to enable high-density integration of chip-based, high-speed optical communication systems[1,2] for datacom, and applications in sensing,[3] computing,[4] and quantum information technology.[5,6] In this context, among the wide spectrum of nanolasers with different cavity structures, [7] single semiconductor nanowire (NW) lasers have garnered increasing attention thanks to their unique 1D geometry, sub-wavelength dimensions and useful optical mode confinement properties. With their mirror-like end-facets, NWs naturally form ultracompact Fabry-Perot type nanolasers, incorporating both an efficient optical waveguide and active gain medium at the same time.[8,9] They also offer large tolerance to lattice mismatch in bandgap engineering,[10,11] and pathways for direct site-selective monolithic integration on silicon (Si) photonic waveguides and circuits.[12–15] This makes them highly versatile and scalable on-chip

T. Schreitmüller, H. W. Jeong, H. Esmaielpour, P. Schmiedeke, A. Thurn,
A. Ajay, S. Matich, J. J. Finley, G. Koblmüller
Walter Schottky Institute and Physics Department
TUM School of Natural Sciences
Technical University of Munich
Am Coulombwall 4, 85748 Garching, Germany
E-mail: tobias.schreitmueller@wsi.tum.de;
gregor.koblmueller@wsi.tum.de

C. E. Mead, L. J. Lauhon
Department of Materials Science and Engineering
Northwestern University
2220 Campus Drive, Evanston, IL 60208, USA

M. Ramsteiner
Paul-Drude-Institut für Festkörperelektronik
Leibniz-Institut im Forschungsverbund Berlin e. V.
Hausvogteiplatz 5–7, 10117 Berlin, Germany

M. Döblinger
Department of Chemistry
Ludwig-Maximilians-University Munich
Butenandtstrasse 5–13 (E), 81377 Munich, Germany

sources with only small power consumption due to their sub-μm² footprint.[16]

For the most technologically relevant Si-photonic platform NW-lasers operating in the near-infrared (IR) spectral range (≈820–1550 nm) have received the most attention in research so far. Optically pumped NW-lasers realized using a diverse array of materials systems have been demonstrated over the last decade, including GaAs/AlGaAs,[17–19] InP,[20] InGaAs,[14,21] InAs/InAsP[22] and GaAs/GaAsP.[23] Thanks to their suitable emission wavelengths, lasing characteristics were intensely studied with respect to the external photonic environment, for example by exploring ultrafast external modulation[14,24,25] and all-optical switching dynamics[26] in Si photonic circuits, but also regarding their intrinsic properties related to material gain and resonator quality. Here, much emphasis has been placed on tuning gain and lasing wavelength, for example, by embedding quantum well (QW) and quantum dot/disk (QD) heterostructures as active gain media,[11,16,22,27–30] identifying the role of surface passivation on radiative efficiency,[31,32] as well as dimensional parameters and end-facet quality on lasing metrics.[33,34] More recently, also large-scale statistical analysis of NW-lasers has become available to better discern geometrical from material parameters in describing lasing threshold and mode spectra characteristics.[32]

Another important, but far less explored factor is the material quality of the active region itself, where various types of defects and impurities that form during NW-laser synthesis impose critical influences on carrier density, trap states, and radiative efficiency. For example, extended dislocation defects emerging at the interfaces of QW-based active regions under highly lattice-mismatched growth have detrimental effects on optical quality[35] and even prevent observation of lasing, as seen in for example, coaxial InGaAs-AlGaAs/GaAs MQW-based NW lasers.[28] Likewise, the radiative efficiency of III-V NW-lasers can be heavily impacted by intentional doping. In this context, first examples have shown that excess p-type (i.e., zinc) doping modifies the surface recombination dynamics in unpassivated GaAs NW-lasers, enabling lasing operation even without the need of surface passivation.[33,37]

Besides surface effects, doping is expected to play a key role for future electrically injected laser diodes, that only exist for deep-ultraviolet (DUV) NW-lasers so far,[7,38] but still need to be developed for near-IR to telecom band NW-lasers. Depending on the design of the active region, the materials system, and envisioned performance metrics, device active regions are often intentionally or unintentionally doped, as is also the case for many traditional III-V planar heterostructure laser diodes. For example, intentional n-type doping (Si or Te doping) has been used in coupled QWs of AlInGaAs/GaAs double-QW-lasers,[39] GaInP-AlGaInP MQW-based laser diodes,[40] or single-QW GaAs/AlGaAs separate confinement heterostructure (SCH) lasers,[41] to favorably manipulate threshold current density. Other examples exploit p-type doping of active regions in InGaAs/InP QW-lasers or InAs/GaAs QD-lasers to increase material gain.[42,43] In cases of unintentionally doped active regions, dopant diffusion from adjacent carrier injection regions, causing displacement of p-n junctions, has long been known a substantial problem in the processing of AlGaAs/GaAs laser diode structures.[44] Dopant diffusion is also an issue in III-V NWs (for example GaAs NWs), as has been observed for a variety of dopant elements.[45–47] The pres-

ence of point defects, either intrinsic or mediated by excess doping, can further aggravate dopant redistribution, and even lead to diffusion-induced layer disordering, seen in for example Si-doped AlGaAs/GaAs MQW structures.[48] Furthermore, point defects, such as vacancies, were found in large quantities in GaAs-based NWs, even without doping.[49] Such defects will become prominent centers for non-radiative recombination processes in future electrically pumped NW-laser diodes, particularly in optimized NW structures that are free from extended defects and have passivated surfaces.
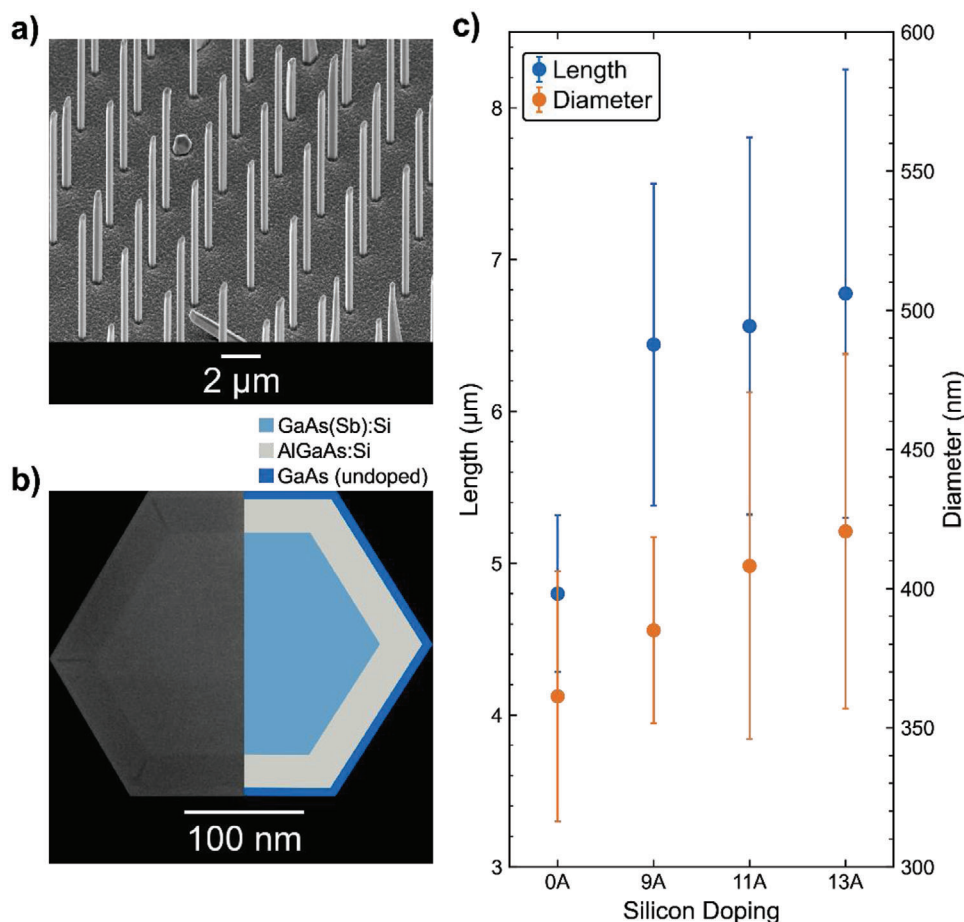
Against this background, there is clear motivation to understand the role of dopants and associated point defects on the lasing performance of III-V NW-lasers. We investigate here such a scenario for the simple case of intentionally Si-doped GaAs(Sb)-AlGaAs core-shell NW-lasers, under the common situation of passivated surfaces. This facilitates the exploration of the intrinsic influence of impurity-induced vacancy-defects on the bulk radiative versus non-radiative carrier recombination dynamics of buried active gain media. Thereby, our work addresses different aspects than those previously studied in other doped GaAs NW-lasers.[33,37] In particular, we reveal how compensating deep-level point defects induced by n-type dopants impact key lasing metrics, such as lasing threshold, and demonstrate how they advantageously affect the temperature stability through modified non-radiative Auger recombination processes. These studies, which are further enabled by a new surfactant-mediated non-catalytic growth scheme, provide, thus, important insights into technologically relevant regimes of lasing operation at elevated temperatures.

Employing Si dopants as intentional impurities for our study of GaAs-based NW-lasers, is motivated by several other key factors, beyond those discussed above: Si dopants exhibit a high incorporation ratio for realizing n-type GaAs (especially in planar thin films), and furthermore, offer a great wealth of well-studied point defect complexes created under excess doping.[50–52] Since Si is an amphoteric impurity, it can, however, also induce p-type doping under specific growth conditions. This is observed particularly for Si-doped GaAs NWs grown by traditional vapor-liquid-solid (VLS) growth processes.[53–55] In contrast, majority n-type conduction with high free carrier densities (10^{18}–10^{19} cm^{-3}) is realized under vapor-solid (VS) selective area growth (SAG), demonstrated by metal-organic vapor phase epitaxy (MOVPE)[56,57] or molecular beam epitaxy (MBE).[58] Si dopants were recently also found to minimize size distribution and enhance array uniformity in VS-SAG of GaAs NWs.[59]

However, both Si-doped and undoped GaAs NWs grown by VS-SAG type processes exhibit limited length,[59,60] which challenges the development of low-threshold NW-lasers. In our study, we therefore utilize recently observed antimony (Sb) surfactant-mediated growth enhancement effects[61,62] that are key to develop high-quality GaAs-based NW-lasers with extended cavity lengths.

2. Results and Discussion

All NW-laser structures investigated in this work were grown using MBE-based SAG on SiO₂-templated n-type Si (111) substrates. The approaches adopted result in high NW uniformity and also result in similar n-type conduction and Si-dopant

**ADVANCED
SCIENCE NEWS**

www.advancedsciencenews.com

**ADVANCED
FUNCTIONAL
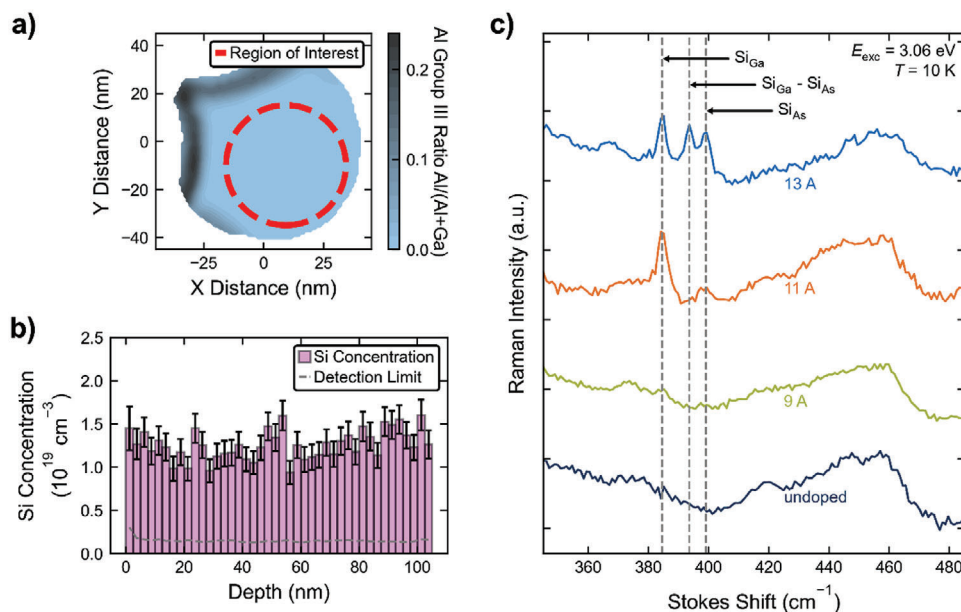MATERIALS**

www.afm-journal.de

Figure 1. a) 45° tilted-view SEM image of an AlGaAs/GaAs-passivated GaAs(Sb) NW array under a Si-dopant flux of 13A; b) Corresponding cross sectional STEM-HAADF image and schematic illustration of a single NW, obtained from the same NW array; c) Average length (blue) and diameter (orange) of the investigated NW-lasers in dependence of the Si-dopant flux (0–13 A). Error bars represent the standard deviation obtained from a statistical analysis of ≈20 NW-lasers, measured for each sample in a dispersed geometry on sapphire substrate.

induced point defect structure[58] as in planar layers. The NWs were grown for a fixed growth time (150 min) under high V/III ratio to create several-μm long and few-hundred-nm thick Si-doped GaAs(Sb) cores as the nanolaser active region, that were further overgrown by a 25 nm thin $Al_{0.15}Ga_{0.85}As$ (Si-doped) passivation layer and a 7 nm thin GaAs cap. Details about growth conditions and substrate preparation can be found in the Experimental Section. The role of antimony added during the growth was to exploit its surfactant action under low Sb supply.[60,61] This enables NW-lengths in excess of 5 μm (needed to reduce the impact of mirror losses), while maintaining optimized aspect ratio for good mode confinement.[17,18] Otherwise, Sb-free GaAs NWs as grown by MBE suffer from limited length due to early growth termination, especially for the undoped case.[59–61] The Sb-content in these NWs is very low (≈1–2%)[60] such as to imitate the Si-dopant incorporation behavior of Sb-free n-type GaAs NWs.[58] Moreover, under such small Sb quantities the NWs exhibit a phase-pure zincblende (ZB) structure with only twin domains present.[60,61] Si doping was controlled by varying the current applied to the employed thermal sublimation source. Here, a current of, for example, 13 A corresponds to a Si-flux of ≈1.6×10^{12} cm^{-2} s^{-1}[62] and the Si dopant flux has an exponential dependence on the heating

current. For reference, a change in heating current from 9 to 11 A, and to 13 A results in an increase in the Si dopant concentration from 5×10^{17} cm^{-3} to 2×10^{18} cm^{-3}, and to 1.4×10^{19} cm^{-3} in planar Si-doped GaAs thin films (growth rate of ≈1 μm hr^{-1}).[62] Similar values are also obtained for our investigated GaAs(Sb):Si NWs, as discussed below.

We continue by presenting morphological details of the Si-doped GaAs(Sb) NWs grown with Si-fluxes varied from 9 to 13 A. **Figure 1a** shows a representative scanning electron microscopy (SEM) image of the obtained AlGaAs/GaAs-passivated GaAs(Sb):Si NW arrays, for a Si-flux of 13 A. A cross sectional STEM-HAADF (scanning transmission electron microscopy – high angle annular dark field) image recorded from a single NW from the same sample, prepared by focused ion beam milling, is also presented in Figure 1b. The image illustrates the expected core-shell configuration, i.e., ≈250 nm wide GaAs(Sb):Si core and ≈30 nm thick AlGaAs / 7 nm thick GaAs passivation. Further SEM images of other NW arrays grown under different Si-fluxes (9 and 11 A), as well as an undoped reference can be found in the Supporting Information, Figure S1. We find that with increasing Si-flux the NW yield and array uniformity increases, giving a yield of >90% with lowest variation in NW length and diameter for

**ADVANCED
SCIENCE NEWS**

www.advancedsciencenews.com

**ADVANCED
FUNCTIONAL
MATERIALS**

www.afm-journal.de

Figure 2. a) 2D contour plot showing the spatial variation of the Al concentration in a highly doped (13 A) NW at a radial cross section recorded near the top of a NW. The red circle delineates the region of interest in the center of the NW from which the axial plot of the Si concentration in b) was extracted; c) Raman spectra of Si local vibrational modes (LVM) in GaAs(Sb):Si NW arrays grown under different Si-fluxes (9–13 A). An undoped GaAs(Sb) NW sample is also included for reference. Peaks of LVMs at 383, 394 and 399 cm^{-1} correspond to Si dopants on Ga-site, Si_{Ga}-Si_{As} pair clusters and Si dopants on As-site, respectively.
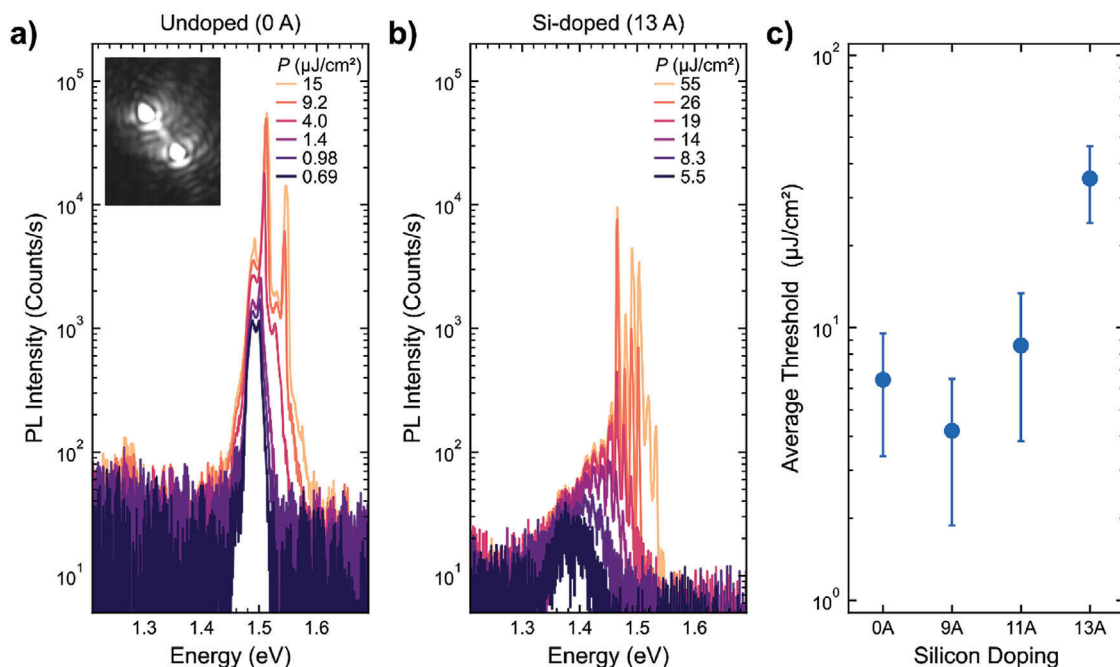
highest doping (Si = 13 A). Any observed NW size variation can be related to the underlying twin-induced growth mechanism, which is a stochastic process, consistent with recent observations in SAG-type GaAs NWs.[59,63]

Regardless of Si-dopant flux the NWs are terminated by a top facet structure that consists of combinations of {111} and inclined {$\bar{1}\bar{1}0$} facets, which are typical for the underlying VS growth mode.[59,63,64] Likewise, the crystal structure remains unaltered by Si doping and is characterized by a ZB-phase with a large density of twin defects for both undoped and Si-doped NWs (see Figure S2, Supporting Information). To further emphasize the influence of Si doping on the NW growth, the average lengths and total diameters of the investigated NW-lasers are presented in Figure 1c. Here, the analysis was performed on NW-lasers removed from the growth substrate in a lying geometry to later correlate the dimensional parameters with lasing properties of individual NW-lasers probed by PL (see discussion of Figure 3). As obvious, undoped NWs exhibit the shortest average length of 4.8 ± 0.5 μm, which increases with Si-doping to 6.8 ± 1.5 μm (13 A). The total diameter of the NWs (incl. passivation) increases as well, from 361 ± 45 nm to 421 ± 64 nm. Together, the evolution in length and diameter yields a continuous increase in aspect ratio with dopant flux from ≈13 (undoped NW-laser) to ≈16 (highly Si-doped NW-laser, 13 A), reflecting the typical trend for the underlying growth technique under Si-doping.[59]

To quantitatively explore the incorporation of Si dopants into the NWs, local electrode atom probe tomography (APT) was performed on highly doped (13 A) samples to provide an upper bound for the Si doping density. Since APT requires a relatively thin specimen, reference NWs were used that were grown under similar conditions but with shorter growth time (75 min) to limit the total diameter of the NWs to less than 130 nm. Details

about the sample preparation methods, as well as the APT experiments are reported in the Methods section. **Figure 2a** shows a 2D contour plot of a radial cross section recorded in the upper region of a NW, illustrating the spatially resolved Al content. The contour plot was extracted from a fully 3D data set, with a typical 3D reconstructed image of a NW shown in the Supporting Information (Figure S3). Despite the limited field of view, this allows for an identification of the hexagonal NW core in the blue region and the first parts of the AlGaAs passivation layer in the darker regions towards the edges. To measure the concentration of incorporated Si atoms in the core, an axial scan was performed in the region marked by the red circle. The Si concentration is presented in Figure 2b for a depth of 100 nm. The concentration shows slight variations along the NW axis and varies between ≈1 × 10^{19} cm^{-3} and ≈1.5 × 10^{19} cm^{-3}; the variations are similar to the experimental uncertainty, and the average value is well above the detection limit of ≈0.2 × 10^{19} cm^{-3} (marked by the dashed line in the figure). In addition, analysis of the radial distribution function (RDF) was performed to characterize cluster formation of Si dopants within the same region (see Figure S4, Supporting Information). Hereby, an RDF value (pairing probability) of 1 reflects a homogeneous Si spatial distribution, while higher values imply the emergence of Si-Si pair complexes. The analysis clearly reveals RDF > 1, and, thus, the presence of Si-Si pairing interaction (similar to Be pairing observed in recent work about Be-doped GaAs NWs[65]). To further correlate Si-doping flux with doping density, as well as lattice site occupation and associated pairing complexes, we performed resonant Raman scattering on as-grown NW arrays similar to those shown in Figure 1a. Due to the limited probing depth of ≈10 nm, no AlGaAs/GaAs passivation layers were grown around these NWs. The experiments were conducted at a temperature of 10 K in a continuous-flow

**ADVANCED
SCIENCE NEWS**
www.advancedsciencenews.com

**ADVANCED
FUNCTIONAL
MATERIALS**
www.afm-journal.de

Figure 3. a) Semi-logarithmic µPL spectra of a single undoped GaAs(Sb) NW-laser at 10 K for different pump fluences. The first lasing peak appears at 1.505 eV at a threshold pump fluence of 3 ± 1 µJ cm^{-2}. The inset shows a CCD image of the NW pumped above threshold showing typical interference fringes in the emission from the end facets; b) Comparative spectra of a single highly Si-doped (13 A) GaAs(Sb) NW-laser probed under the same conditions. The NW exhibits lasing at lower energy (first lasing peak at $\approx$1.46 eV) with a higher lasing threshold of 15 ± 3 µJ cm^{-2} compared to the undoped NW; c) Statistical distribution of average lasing thresholds as a function of Si-doping at 10 K, obtained for $\approx$20 NW-lasers per sample.

He- cryostat in backscattering geometry using a SureLock LM series diode laser at a wavelength of 405 nm in resonance with the E_1 gap of GaAs.[66,67] The recorded Raman spectra are shown in Figure 2c for NW arrays grown under different Si doping currents of 9, 11, and 13 A, together with an undoped reference for comparison. The dashed lines indicate the frequencies of Si-related local vibrational modes (LVMs), which directly refer to the incorporation sites of Si dopant atoms on Ga-sites (donors, 383 cm^{-1}), on As-sites (acceptors, 399 cm^{-1}), and as Si_{Ga}-Si_{As} pair complexes (394 cm^{-1}).[68]

As expected, Si related LVMs are absent in the undoped sample, whereas a weak Si_{Ga}-LVM peak at 385 cm^{-1} can be identified for the lightly doped (9 A) sample. The detection limit for Si-LVMs is $\approx$10^{18} cm^{-3},[69] providing a lower bound for the n-type doping density of these lightly doped NWs. For medium doping of 11 A, the intensity of the Si_{Ga} related LVM clearly increases, suggesting higher n-type doping density. However, a second weak peak at 399 cm^{-1} is observed, indicating residual incorporation of Si atoms on undesired group-V (As/Sb) lattice sites as acceptors. This mode was also observed for Sb-free GaAs:Si NWs[58] confirming the amphoteric nature of Si dopants in GaAs at high concentrations. For the highest doping (13 A), the LVM-peaks associated with the occupation on Si_{As} sites and Si_{Ga}-Si_{As} pair complexes become even more prominent. This degree of self-compensation exceeds that observed in comparably doped Sb-free GaAs:Si NWs,[58] and could be related to the presence of Sb during growth. At the highest doping level nearest-neighbor Si_{Ga}-Si_{As} pair complexes emerge, which confirms the APT data shown in Figure S4 (Supporting Information) and provides clear indication of overdoping.[70] Such Si_{Ga}-Si_{As} pair complexes are typically

accompanied by large densities of Ga-vacancy (V_{Ga}) defects,[51,71] which are acceptor-like point defects in n-type GaAs and further contribute to the autocompensation.[72] Below, we provide direct evidence for these defect complexes as they dominate the emission characteristics of highly Si-doped GaAs(Sb) NWs.

In **Figure 3** we present pump-fluence dependent micro-PL measurements recorded from single passivated GaAs(Sb) NW-lasers for different Si-doping levels. The data were recorded at 10 K using pulsed optical excitation on NWs dispersed onto a sapphire (Al$_2$O$_3$) substrate to provide a high refractive index contrast at the end facets.[11] Additional details are presented in the methods section. Looking first at the undoped NW reference, at low pump fluence the spectrum is dominated by a distinct spontaneous emission peak centered $\approx$1.49 eV. The peak is slightly redshifted compared to the usual zincblende (ZB) GaAs PL peak energy of 1.51 eV, consistent with previous results obtained on GaAs(Sb) NWs.[61] The peak shift is mainly due to the slightly reduced bandgap energy of the GaAs(Sb) NW, having an Sb-content of $\approx$1–2%, but likely also the microstructure that consists of a high density of rotational twins.[61]

Such twin domains induce type-II interfaces and are well known to cause a slight redshift in the PL emission, regardless of the growth technique and mode used.[32,61,73] To provide an estimate of the intrinsic carrier density of the undoped NW, we fit the emission spectrum at lowest pump fluence to extract an upper bound of the intrinsic n-type carrier density of $\approx$4($\pm$ 1) $\times$ 10^{17} cm^{-3}. By increasing the pump fluence above a certain threshold (>3.0 µJ cm^{-2}), we observe a sharp peak at 1.50 eV that arises with a significantly higher intensity than the spontaneous emission background. The intensity of this peak increases
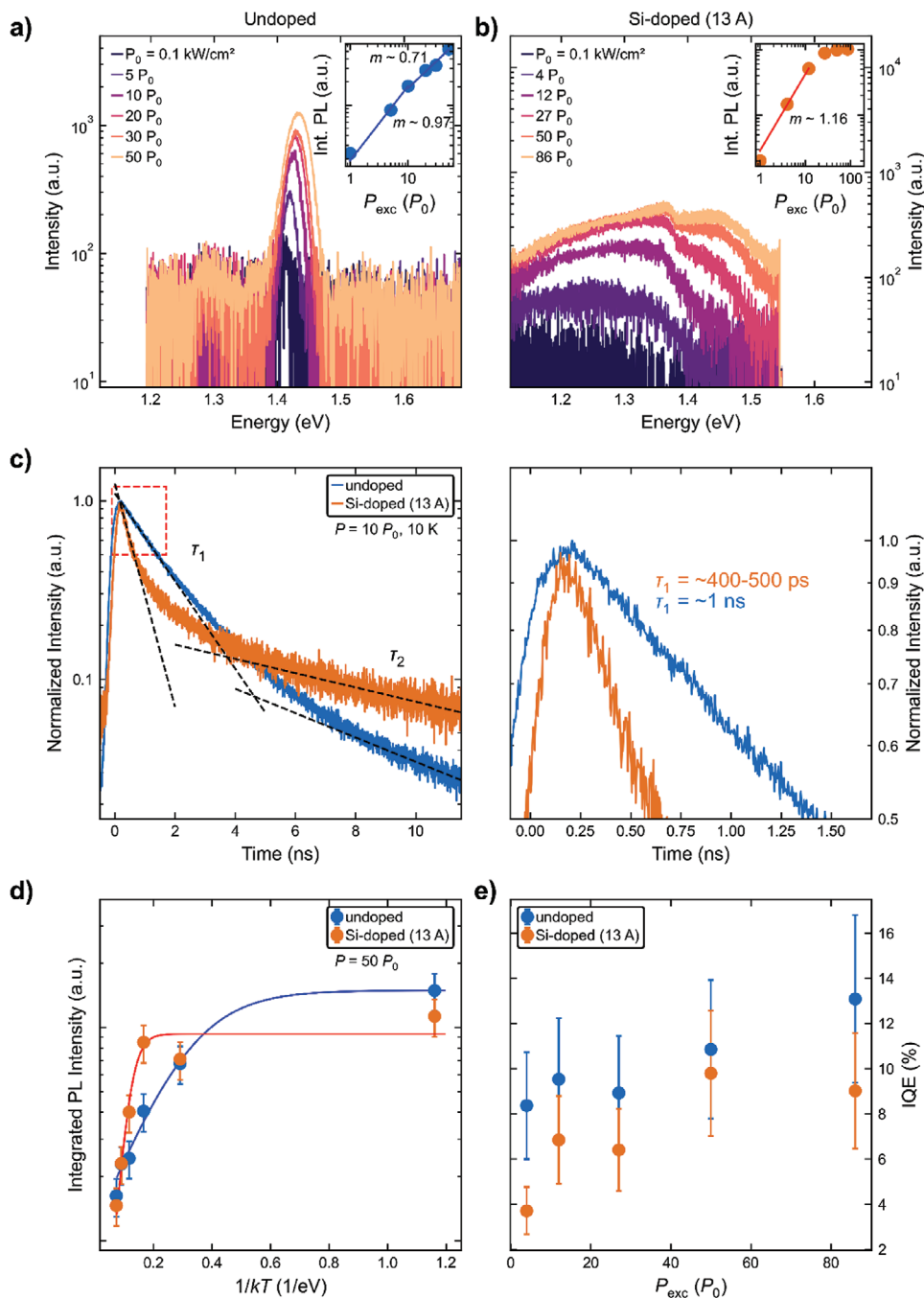
strongly with pump fluence above threshold, indicative of lasing emission from the single NW.[11–23] Furthermore, at higher pump fluence >7.3 µJ cm⁻² a second sharp peak at 1.56 eV appears, suggesting that more than one mode in the FP-resonator cavity contributes to lasing. Note, the presence of longitudinal FP modes is directly observed by the modulation of the spontaneous emission background, as seen also in many other NW-lasers (cf. Figure 3b and Supporting Information). The coherent light emission that outcouples at the end-facets of the NW-laser above threshold was further verified by the spatial interference pattern, as recorded with a Si charge coupled device (CCD) camera (see inset of Figure 3a). The remarkably low lasing threshold of only ≈3 ± 1 µJ cm⁻² observed for this NW is among the lowest ever reported for III-V NW-lasers[11,13,15,19,27,31,33,36] (see also, Figure S5, Supporting Information, for threshold analysis). This attests to the high optical and structural quality of the Sb-mediated GaAs(Sb) NWs grown under the VS-SAG process.[60,61] For comparison, typical pump-fluence dependent PL spectra of a highly Si-doped (13 A) GaAs(Sb) NW laser are shown in Figure 3b and in Figure S6 (Supporting Information). Several key differences with respect to the undoped case (or slightly doped NWs, see Figure S7, Supporting Information) become obvious when analyzing the spectra: First, the emission is strongly redshifted and broadened, with a peak emission centered near 1.37 eV. The peak emission is further shifted toward lower energies (<1.35 eV) for the lowest investigated pump fluences (see also **Figure 4**). By increasing pump fluence, a significant broadening of the emission is observed indicative of state-filling of the deep defect centers that dominate the spontaneous emission. Similar effects have been previously seen in Si-doped GaAs NWs.[58] Broad defect bands between ≈1.25 – 1.4 eV are directly associated with Si-induced point defect centers in GaAs, such as donor-acceptor complexes, for example Si-donor/Ga-vacancy complexes (Si_{Ga}-V_{Ga}), Si-acceptor/As-vacancy centers (Si_{As}-V_{As}), or As_{Ga}-Si_{Ga} donor-donor pair complexes.[48,51,52,58] In particular, we tentatively suggest that the Si_{Ga}-V_{Ga} complex is the most prominent defect center since its formation energy is lowest under the employed As-rich growth conditions.[51] This complex was also found to be responsible for self-compensation in heavily Si-doped GaAs[52] and a source for strong non-radiative Shockley-Read-Hall (SRH) recombination.[74]

When further increasing pump fluence beyond ≈14 µJ cm⁻², see Figure 3b, a sharp lasing peak at 1.46 eV appears with an intensity that grows to exceed the spontaneous emission by two orders of magnitude. The main peak energy is further redshifted compared to the undoped NW laser which could be attributed to bandgap narrowing in the highly doped sample additional to the already mentioned influence of twin defects.[75] At even higher pump fluences, several other peaks with varying modal spacing arise, suggesting lasing of additional transversal and longitudinal modes in the NW. Similar to the scheme for the undoped NW-laser, the lasing threshold was determined from the first lasing peak emerging at lowest energy, which results in a threshold pump fluence of 15 ± 3 µJ cm⁻² (see Figure S5, Supporting Information). This value is more than five-fold larger than for the undoped NW-laser, despite the larger NW-length suggesting inferior radiative efficiency. However, support for this conclusion requires analysis from a statistically relevant dataset, since lasing threshold depends also on variations in cavity length, end facet

quality, and other factors.[23,33,34] Thus, in Figure 3c we present comprehensive threshold statistics obtained from ≈20 NW-lasers probed per sample.

The threshold values of lightly to moderately Si-doped NW-lasers are very low and only change by less than 40% with respect to the undoped case, suggesting relatively large tolerance of lasing behavior to Si-doping. The highest Si-doping (13 A) exhibits, however, a much higher average lasing threshold, i.e., 35 ± 11 µJ cm⁻². We note that our data encompasses an arbitrary set of NW-lasers per sample, with no specific selection regarding their lengths or diameters. Hence, any variations in length, diameter and/or mode set are captured within the deviation in threshold (marked by the error bars) for each of the given samples. Taking the dimensional analysis of Figure 1c into consideration, we can make certain assessments though of the overall observed trends in lasing threshold. For example, the slightly reduced threshold in lightly doped NW-lasers (9 A) is mostly representing the substantially increased NW-length with respect to the undoped case (0 A). For higher doping (11 A, 13 A) the average NW-length increases, however, only marginally with respect to lightly doped NW-lasers, but their corresponding thresholds are significantly increased, especially for highest doping (13 A). To determine whether Si dopants and defect complexes are responsible for the increased threshold, we first consider other factors that could produce significant increases in the lasing threshold. We can first rule out changes in end-facet quality, since the quality of the growth facet structure does not deteriorate with Si-doping[60,61] (see also Figure S1, Supporting Information). We also directly measured the lengths and diameters of the probed NW-lasers (using SEM after optical analysis) in an attempt to more closely observe any links to the threshold characteristics from the data spread. However, any variations in threshold with geometrical parameters were marginal in comparison to the differences between un- or lightly-doped NWs and highly-doped NWs. For example, as shown in Figure S8 (Supporting Information), for NW-lasers doped at 9 A, the lasing threshold only varies in the range from 2.5 to 5.5 µJ cm⁻² when varying NW-length from 7.7 to 3.7 µm or NW-diameter from 300 to 450 nm. Hence, the remarkably different lasing threshold (>5× larger threshold) found in the presence of large Si-dopant induced defect densities suggests non-radiative recombination becoming very prominent to affect lasing threshold.

To test this hypothesis we performed pump-fluence and temperature-dependent analysis of the spontaneous emission, as well as time-resolved PL characterization to measure carrier lifetimes, and thereby, assess the role of non-radiative recombination. Figure 4a,b compares pump-power dependent PL spectra of the spontaneous emission from an undoped and highly doped NW (13 A) at 10 K. The NWs investigated here were from reference samples grown under identical conditions as the NW-laser structures, but with shorter growth time (reduced length/diameter) to inhibit formation of FP-modes superimposing the spontaneous emission spectra. The spectra were recorded using pump-powers ranging from $P_0 = 10$ µW (0.1 kW cm⁻²) up to ≈85 P_0, to observe the recombination dynamics over nearly two orders of magnitude. Overall, the spectra exhibit similar pump-power dependent characteristics to those shown in Figure 3, but their emission extends further toward lower peak energies due to the much lower excitation levels.

ADVANCED
SCIENCE NEWS

www.advancedsciencenews.com

ADVANCED
FUNCTIONAL
MATERIALS

www.afm-journal.de

Figure 4. Pump-power dependent PL spectra of the spontaneous emission of a) an undoped and b) a highly Si-doped GaAs(Sb) NW (13 A) at 10 K; Insets show the scaling behavior of the integrated PL intensity versus pump-power; c) TRPL data recorded at low pump-power (10 $P_0 = 1$ kW cm^{-2}), illustrating the faster initial decay of the Si-doped NW as compared to the undoped NW, giving a carrier lifetime of $\approx$450 ps versus 1 ns, respectively; d) Temperature dependence of the integrated PL intensity measured in the range of 10–160 K, plotted at a fixed pump-power ($P = 50\ P_0$), as well as e) extracted IQE at 160 K for different pump-power. The undoped NW exhibits higher IQE compared to the Si-doped NW.

Plotting the integrated PL intensity as a function of pump-power reveals the dominant recombination processes from the exponent (m) of the intensity (I) versus pump-power (P) characteristics ($I \propto P^m$). Typical data obtained for the two respective NWs are presented in the insets of Figure 4a,b. According to the conventional ABC-model, the total recombination rate depends

thereby on the contributions from trap-assisted Shockley-Read-Hall (SRH), radiative band-to-band and Auger recombination, respectively.

In this regard, a scaling behavior of the integrated PL intensity versus pump-power that has an exponent of $m = 1$ represents a radiative band-to-band recombination, while slopes of

**ADVANCED
SCIENCE NEWS**

www.advancedsciencenews.com

**ADVANCED
FUNCTIONAL
MATERIALS**

www.afm-journal.de

$m = 2$ and $m = 2/3$ describe non-radiative SRH and Auger recombination, respectively.[76] For the undoped NW, the exponent of the integrated PL versus pump-power is close to $m = 1$ for low pump-powers up to $\approx 10\ P_0$, indicating that radiative recombination is dominant. For higher pump-power, the exponent shows sub-linear behavior ($m \approx 0.7$), and thus illustrates an increased contribution from Auger recombination arising from the higher photogenerated carrier density. In contrast, the highly Si-doped GaAs(Sb) NW, which is dominated by the broad Si-induced point defect emission band, exhibits initially a super-linear exponent of ≈ 1.2. This clearly indicates the presence of non-radiative SRH recombination in the limit of low carrier density. At higher pump-power, the slope becomes strongly sub-linear which reflects gradual saturation of the defect emission, accompanied by an increase in the contribution of Auger recombination.

Further evidence for the trap-assisted SRH recombination in the highly Si-doped GaAs(Sb) NW is gained from time-resolved PL (TRPL) measurements performed on the same NW. Figure 4c shows TRPL data recorded at low excitation power of 10 P_0 at 10 K, in comparison with the undoped NW reference. The data was normalized to the respective peak intensity, hence the rise time of the two samples appears slightly offset. The temporal decay of both NWs is described by a stretched exponential behavior (see left panel). Such behavior is typical for NWs hosting twin defects, which induce long-lived excitonic states (due to indirect type-II transitions) seen in the slow decay component of the exponential tail, whereas the quasi-free continuum states are captured in the fast, initial decay characteristics.[60,61,77] As such, the stretched exponential can be approximated by a bi-exponential decay to discriminate the lifetimes of twin-related localized excitons (τ_2) from the quasi-free continuum states (τ_1). Since both the undoped and Si-doped NWs contain twin defects with high densities, and only differ via the presence or absence of dopant induced point-defects, we place our carrier lifetime assessment on the fast, initial decay τ_1 of the direct radiative transitions (see right panel). Here, we determine a carrier lifetime of ≈ 1 ns for the undoped NW, which is in good agreement with other data reported for high-quality, passivated GaAs NWs.[77,78] Significantly faster decay is observed for the highly Si-doped NW, leading to a carrier lifetime of ≈ 400-500 ps. This directly reflects the enhanced SRH recombination process, as expected from the inferior material quality, i.e., much larger point defect density in this NW.
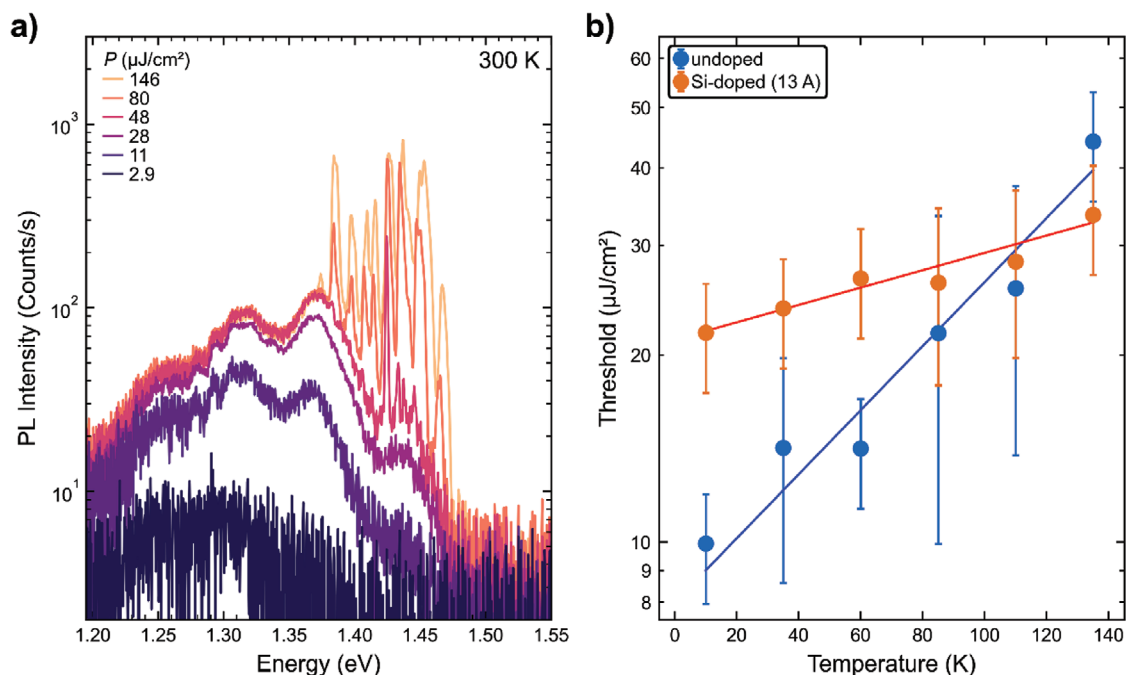
Single-wire PL measurements were further performed at elevated temperature (up to 160 K) to highlight the differences in material quality of doped and undoped NWs, in particular by estimating their internal quantum efficiency (IQE). Here, we applied the method of dividing the integrated PL intensity (I_{PL}) at highest temperature (160 K in this case) by that at lowest temperature (10 K), to estimate the IQE at different pump-powers (assuming a hypothetical IQE of 100% at 10 K where radiative recombination prevails).[79] Spectra recorded at different temperatures are shown in the accompanying Supporting Information, Figure S9, while a typical plot of the integrated intensity over inverse temperature is presented in Figure 4d. A comparison of the two datasets already suggests lower IQE in the doped NW, as with higher temperature the intensity drops much more rapidly in the doped case and even vanishes for temperatures greater than 160 K. Figure 4e summarizes the resulting IQE at 160 K as a function of pump-

power. Discussing first the undoped NW, we observe an IQE that varies between ≈ 8–13% with pump-power. We emphasize that the data is most reliable at low pump-power, since recombination is dominated by radiative processes (cf. Figure 4a). For the Si-doped NW, an estimate of the IQE is less straightforward since the underlying SRH recombination limits the radiative efficiency at low temperature, i.e., the IQE cannot be reliably calculated via $I_{PL}(160\ K)/I_{PL}(10\ K)_{doped}$. Instead, we divided the integrated intensity of the doped NW at 160 K by that of the undoped NW at 10 K, to better illustrate the change in IQE under radiative recombination. As a result, the IQE values for the highly doped NW are by a factor of ≈ 1.5–2.2 lower compared to the undoped NW, confirming the detrimental impact of the large density of point defect states on quantum efficiency.

Finally, we investigated the temperature dependence of the NW lasing characteristics, to identify their performance metrics in relation to the underlying material quality. Pump-fluence dependent spectra recorded at room-temperature (300 K) are shown in **Figure 5a** for a typical Si-doped GaAs(Sb) NW-laser at highest doping level (13 A), as well as in Figure S10 (Supporting Information). Remarkably, despite the presence of significant dopant-induced defects (seen by the broad defect emission band from ≈ 1.2–1.4 eV in the spontaneous emission), clear lasing behavior is observed. The main peak in the lasing emission emerges at ≈ 1.41 eV, while several other lasing peaks around the central peak occur at pump-fluences further above threshold. The threshold fluence of this NW-laser was determined from the emergence of the first lasing peak, yielding a value of 53 $\pm$ 17 µJ cm^{-2}. Compared to measurements performed at 10 K (see Figure 3), both the spontaneous emission and the band of lasing peaks are red-shifted by ≈ 70–80 meV at 300 K, reflecting the expected bandgap reduction of the GaAs(Sb) NW. Excess heating of the NW-laser (for example by the pump laser) is negligible, since with increased pump-fluence slightly blue-shifted emission is observed, indicative of state-filling.

To further investigate the temperature stability of the NW-lasers, the scaling behavior of the lasing threshold was evaluated over an extended temperature region. Figure 5b compares typical data of the threshold versus temperature dependency of a highly Si-doped NW-laser with that of an undoped NW-laser, plotted on a semi-logarithmic scale. This comparison illustrates interesting differences; first, the undoped NW-laser has much lower lasing threshold at low temperature (10 K), similar to the observations in Figure 3. However, the lasing threshold rises more rapidly with temperature in the undoped NW-laser as compared to the highly Si-doped NW-laser. For the two NW-lasers, the threshold of the undoped NW-laser even surpasses the one of the doped NW-laser for temperatures exceeding 120 K. This behavior is consistently observed in several other NW-lasers that were analyzed from each sample. To quantify these peculiar differences, we derived the characteristic temperature of the respective NW-lasers from the exponential dependency between lasing threshold and temperature, i.e., $P_{th} = P_0 \cdot e^{T/T_0}$.[18,80–82] For the undoped NW-laser presented in Figure 5b, where the lasing threshold is more sensitive to lattice temperature, we obtain $T_0 = 84 \pm 10$ K. Data from other undoped NW-lasers are similar, with T_0 varying between $\approx 70 - 130$ K. These relatively low values agree favorably with data reported in literature for undoped bulk GaAs NW-lasers.[18] For the highly Si-doped NW-lasers, we obtain a much higher

**ADVANCED
SCIENCE NEWS**

www.advancedsciencenews.com

**ADVANCED
FUNCTIONAL
MATERIALS**

www.afm-journal.de

Figure 5. a) Pump-fluence dependent PL spectra of a highly Si-doped GaAs(Sb) NW-laser (13 A) at 300 K. The first lasing peak occurs at ≈1.41 eV at a threshold of 53 µJ cm^{-2}, while multimode lasing is observed a higher pump fluences; b) Temperature dependence of the lasing threshold revealing the characteristic temperature T_0 for typical undoped (blue) and highly Si-doped (13 A, orange) NW-lasers.

characteristic temperature, for example, $T_0 = 311 \pm 36$ K for the NW shown in Figure 5b, reflecting the reduced temperature sensitivity.

The exact reasons for the different behavior require additional investigations, but suggest that the net gain needed to obtain threshold and/or the Auger recombination rates, which are known to limit high-temperature lasing performance,[83] are likely to be different. The behavior is further reminiscent of the findings of p-type doped quantum-dot lasers, where larger insensitivity in threshold was observed (at the expense of higher overall threshold), compared to undoped devices.[84–86] Here, the temperature dependence of the Auger recombination process and its modification by acceptor states has been argued as a prime cause for the temperature-insensitive lasing threshold.[84,85] To what extent the strongly self-compensating nature and large densities of acceptor-like vacancy complexes modify the Auger recombination processes in our highly Si-doped GaAs(Sb) NWs is an interesting question to be resolved. Some evidence for a reduced Auger recombination in the highly Si-doped NWs with respect to the undoped NWs might be seen in the carrier (electron) temperature evaluation at threshold. We therefore extracted the carrier temperature (T_e) by modelling the spontaneous emission spectra as a function of pump-fluence, as shown in Figure S11 (Supporting Information).[89] Details about the model that has been used to fit the spontaneous emission spectra are explained in Note S12 (Supporting Information). Hereby, we found that for the same undoped NW as in Figure 5b, the carrier temperature increased from $T_e \approx 160$ K at 35 K to ≈240 K at 135 K. In contrast, the Si-doped NW shown in Figure 5b exhibits hardly any deviation in carrier temperature between 35 and 135 K, with T_e remaining at ≈180 K. The absence of any carrier temperature change hints to-

ward a reduced Auger heating in the Si-doped NWs, that may explain their much lower temperature sensitivity. A rigorous proof of this explanation requires, however, extended studies combining modelling of the microscopic Auger processes in the presence of deep-level traps together with ultrafast pump-probe experiments to reveal the magnitudes of these processes at different temperatures.

3. Conclusion

In conclusion, we demonstrated the material inherent impact of dopant-induced bulk defect states on the lasing properties of GaAs(Sb)-AlGaAs core-shell nanowire (NW) lasers. The NW-lasers studied here were based upon high-quality, phase-pure GaAs(Sb) NWs with extended cavity lengths, facilitated by antimony (Sb) surfactant effects in site-selective vapor-solid growth processes. As impurity-induced defects we explored in particular Si-dopants and their associated point defect complexes (vacancy complexes) since they offer wide tunability in lattice site occupancy due to the amphoteric nature of Si dopants in GaAs. The Si doping density and lattice site occupancy were directly determined using atom probe tomography (APT) and resonant Raman scattering, respectively, while further evidence of deep-level vacancy complexes (≈100–200 meV below bandgap) was obtained from micro-photoluminescence spectroscopy. From pump-power, temperature-dependent, as well as time-resolved studies of the spontaneous emission, we recognized that the large point defect densities under excess doping ([Si]>10^{19} cm^{-3}) resulted in non-radiative Shockley-Read-Hall recombination with substantially reduced carrier lifetime, and at least ≈1.5 to 2-fold lower internal quantum efficiencies (IQE) compared to

**ADVANCED
SCIENCE NEWS**

www.advancedsciencenews.com

**ADVANCED
FUNCTIONAL
MATERIALS**

www.afm-journal.de

undoped reference lasers. The increased non-radiative recombination was directly reflected by an increased lasing threshold behavior (≈one order of magnitude larger threshold) under optical pumping at low-temperature (10 K). However, for wide ranges of Si-doping, i.e., 10^{17} up to mid-10^{18} cm^{-3}, the lasing properties were not affected at all (very low threshold <10 μJ cm^{-2}). Quite remarkably, despite the much lower IQE in highly defective NW-lasers, their temperature stability consistently outperforms undoped NW-laser references, yielding higher characteristic temperature, and lasing at 300 K was also demonstrated with comparatively moderate threshold. Analysis of the carrier temperature at threshold suggests large increases in carrier temperature with rising lattice temperature in undoped NW lasers, indicating substantial Auger recombination, while such behavior appears suppressed in the presence of impurity-induced defect states. These observations point to a great tolerance of key lasing metrics to impurity defects in the GaAs-based NW-laser system, especially at elevated operating temperatures that are relevant for technological applications.

4. Experimental Section

Nanowire Growth: All NWs reported here were grown in an all solid-source molecular beam epitaxy (MBE) system (Veeco Gen-II) using prepatterned n-type Si (111) wafers as substrates. To induce selective area growth (SAG) a 20 nm thin, thermally grown SiO$_2$ mask layer was employed that was patterned by electron beam lithography (EBL), reactive ion etching (RIE) and a buffered hydrofluoric (HF) acid dip.[57–60] The NW core growth followed the same procedures as described in Refs. 59 and 60, except that here a relatively high growth temperature of 685 °C (measured by pyrometer) was used to account for the different substrate doping/resistivity. Highly As-rich conditions with a high V/III ratio of 63 was used, where beam fluxes were supplied by standard effusion cells for Ga, Al and valved cracker cells for As4 and Sb2 species. The core growth was performed for 150 min, with a Ga rate of 0.6 Å s^{-1}, and As- / Sb-BEP (beam equivalent pressure) of 5.5×10^{-5} mbar and 3×10^{-7} mbar, respectively. Subsequent shell growth was completed at a Ga rate of 0.7 Å s^{-1}, an Al rate of 0.124 Å s^{-1}, at 490 °C and a reduced As-BEP of 3.5×10^{-5} mbar, according to optimized growth conditions for {110}-oriented AlGaAs layers.[87,88] The heating current of the Si filament of the Si-sublimation source was 9 A during AlGaAs shell growth. To prevent oxidation of this shell a 7 nm-thin GaAs cap was grown in the end at a growth temperature of 580 °C.

Atom Probe Tomography: For APT analysis, a reference NW sample was used in order to meet the specimen thickness requirements for successful measurements. NWs with a maximum total diameter of ca. 130 nm were grown simply by adjusting the growth time of the Si-doped core (doped at 13 A) to 75 min. Furthermore, an AlGaAs shell was employed without any Si-doping and increased the Al-content to 30%, to enhance material contrast between core and shell. In total, this resulted in ca. 3.8 μm long AlGaAs/GaAs-passivated GaAs(Sb):Si NWs with a mean diameter of ca. 130 nm. Individual nanowires were mounted on tungsten wires using platinum-carbon welds in a FEI Helios dual-beam focused ion-beam (FIB) microscope. APT analysis was performed by a LEAP 5000XS (Cameca, Madison, WI) using a 355 nm laser with 0.8 pJ laser energy and a 250 kHz pulse rate. The sample was run under a background pressure of 3×10^{-11} Torr and 30 K stage temperature using a 3% ion detection rate. IVAS 3.8.6 was used to reconstruct the APT data on which the concentration values were based.

Photoluminescence Spectroscopy: All optical characterization was performed using micro-photoluminescence (μ-PL) spectroscopy of single NWs dispersed on a sapphire substrate and excited in lying geometry with a pulsed Ti:Sapphire laser at 736 nm, a repetition rate of 82 MHz and a pulse length of ≈200 fs. Excitation and detection were simultaneously realized through a 50×/0.42 numerical aperture (NA) objective giving an excitation spot size of ≈20 μm which was larger than the NW length allowing for homogeneous pumping of the whole wire. PL emission was collected either from a small spot at one of the end-facets for NW-laser characterization (as illustrated in Figure 3) or from the central region when probing mainly the spontaneous emission characteristics (as discussed in Figure 4). Measurements were conducted under vacuum conditions in a liquid helium cooled flow cryostat at temperatures variable from 10 K to room temperature (300 K). Time-resolved PL (TRPL) measurements were facilitated by time correlated single photon counting (TCSPC) using a single-photon Si avalanche diode (SPAD) with a time resolution of <365 ps and a PicoHarp 300 module. The TRPL data was obtained over the entire PL spectral range – hence, the emission was not spectrally resolved, while fitting of exponential decay was convoluted with the instrument response function (IRF) of the experimental system.

Supporting Information

Supporting Information is available from the Wiley Online Library or from the author.

Conflict of Interest

The authors declare no conflict of interest.

Data Availability Statement

The data that support the findings of this study are available in the supplementary material of this article.

[1] C. Sun, M. T. Wade, Y. Lee, J. S. Orcutt, L. Alloatti, M. S. Georgas, A. S. Waterman, J. M. Shainline, R. R. Avizienis, S. Lin, B. R. Moss, R. Kumar, F. Pavanello, A. H. Atabaki, H. M. Cook, A. J. Ou, J. C. Leu, Y.-H. Chen, K. Asanovic, R. J. Ram, M. A. Popovic, V. M. Stojanovic, *Nature* **2015**, *528*, 534.

[2] A. Y. Liu, J. Bowers, *IEEE J. Sel. Top. Quantum Electron.* **2018**, *24*, 6000412.

[3] A. Karabchevsky, A. Katiyi, A. S. Ang, A. Hazan, *Nanophotonics* **2020**, *9*, 3733.

[4] D. Liang, A. Roshan-Zamir, Y.-H. Fan, C. Zhang, B. Wang, A. Descos, W. Shen, K. Yu, C. Li, G. Fan, G. Kurczveil, Y. Hu, Z. Huang, M. Fiorentino, S. Kumar, S. M. Palermo, R. G. Beausoleil, *J. Lightwave Technol.* **2020**, *38*, 3322.

[5] J. Wang, S. Paesani, Y. Ding, R. Santagati, P. Skrzypczyk, A. Salavrakos, J. Tura, R. Augusiak, L. Mancinska, D. Bacco, D. Bonneau, J. W. Silverstone, Q. Gong, A. Acín, K. Rottwitt, L. K. Oxenløwe, J. L. O'brien, A. Laing, M. G. Thompson, *Science* **2018**, *360*, 285.

[6] A. Chanana, H. Larocque, R. Moreira, J. Carolan, B. Guha, E. G. Melo, V. Anant, J. Song, D. Englund, D. J. Blumenthal, K. Srinivasan, M. Davanco, *Nat. Commun.* **2022**, *13*, 7693.

[7] K. Ren, K. Li, Z. Fang, F. Feng, *Laser Photon. Rev.* **2023**, *17*, 2200758.

[8] C. Couteau, A. Larrue, C. Wilhelm, C. Soci, *Nanophotonics* **2015**, *4*, 90.

[9] S. W. Eaton, A. Fu, A. B. Wong, C.-Z. Ning, P. Yang, *Nat. Rev. Mater.* **2016**, *1*, 16028.

[10] L. Balaghi, G. Bussone, R. Grifone, R. Hübner, J. Grenzer, M. Ghorbani-Asl, A. V. Krasheninnikov, H. Schneider, M. Helm, E. Dimakis, *Nat. Commun.* **2019**, *10*, 2793.

[11] P. Schmiedeke, A. Thurn, S. Matich, M. Döblinger, J. J. Finley, G. Koblmüller, *Appl. Phys. Lett.* **2021**, *118*, 221103.

[12] R. Chen, T.-T. D. Tran, K. W. Ng, W. S. Ko, L. C. Chuang, F. G. Sedgwick, C. Chang-Hasnain, *Nat. Photonics* **2011**, *5*, 170 .

[13] B. Mayer, L. Janker, B. Loitsch, J. Treu, T. Kostenbader, S. Lichtmannecker, T. Reichert, S. Morkötter, M. Kaniber, G. Abstreiter, C. Gies, G. Koblmüller, J. J. Finley, *Nano Lett.* **2016**, *16*, 152.

[14] H. Kim, W.-J. Lee, A. C. Farrell, J. S. D. Morales, P. Senanayake, S. V. Prikhodko, T. J. Ochalski, D. L. Huffaker, *Nano Lett.* **2017**, *17*, 3465.

[15] T. Stettner, T. Kostenbader, D. Ruhstorfer, J. Bissinger, H. Riedl, M. Kaniber, G. Koblmüller, J. J. Finley, *ACS Photonics* **2017**, *4*, 2537.

[16] F. Lu, I. Bhattacharya, H. Sun, T.-T. D. Tran, K. W. Ng, G. N. Malheiros-Silveira, C. Chang-Hasnain, *Optica* **2017**, *4*, 717.

[17] D. Saxena, S. Mokkapati, P. Parkinson, N. Jiang, Q. Gao, H. H. Tan, C. Jagadish, *Nat. Photonics* **2013**, *7*, 963.

[18] B. Mayer, D. Rudolph, J. Schnell, S. Morkötter, J. Winnerl, J. Treu, K. Müller, G. Bracher, G. Abstreiter, G. Koblmüller, J. J. Finley, *Nat. Commun.* **2013**, *4*, 2931.

[19] J. Ho, J. Tatebayashi, S. Sergent, C. F. Fong, S. Iwamoto, Y. Arakawa, *ACS Nano* **2015**, *2*, 165.

[20] W.-Z. Xu, F.-F. Ren, D. Jevtics, A. Hurtado, L. Li, Q. Gao, J. Ye, F. Wang, B. Guilhabert, L. Fu, H. Lu, R. Zhang, H. H. Tan, M. D. Dawson, C. Jagadish, *Nano Lett.* **2018**, *18*, 3414.

[21] H. Kim, A. C. Farrell, P. Senanayake, W.-J. Lee, D. L. Huffaker, *Nano Lett.* **2016**, *16*, 1833.

[22] G. Zhang, M. Takiguchi, K. Tateno, T. Tawara, M. Notomi, H. Gotoh, *Sci. Adv.* **2019**, *5*, eaat8896.

[23] S. A. Church, N. Patel, R. Al-Abri, N. Al-Amairi, Y. Zhang, H. Liu, P. Parkinson, *Adv. Opt. Mater.* **2023**, *11*, 2202476 .

[24] B. Mayer, A. Regler, S. Sterzl, T. Stettner, G. Koblmüller, M. Kaniber, B. Lingnau, K. Lüdge, J. J. Finley, *Nat. Commun.* **2017**, *8*, 15521.

[25] M. Takiguchi, A. Yokoo, K. Nozaki, M. D. Birowosuto, K. Tateno, G. Zhang, E. Kuramochi, A. Shinya, M. Notomi, *APL Photonics* **2017**, *2*, 046106.

[26] M. Takiguchi, N. Takemura, K. Tateno, K. Nozaki, S. Sasaki, S. Sergent, E. Kuramochi, T. Wasawo, A. Yokoo, A. Shinya, M. Notomi, *ACS Photonics* **2020**, *7*, 1016.

[27] J. Tatebayashi, S. Kako, J. Ho, Y. Ota, S. Iwamoto, Y. Arakawa, *Nat. Photonics* **2015**, *9*, 501.

[28] T. Stettner, A. Thurn, M. Döblinger, M. O. Hill, J. Bissinger, P. Schmiedeke, S. Matich, T. Kostenbader, D. Ruhstorfer, H. Riedl, M. Kaniber, L. J. Lauhon, J. J. Finley, G. Koblmüller, *Nano Lett.* **2018**, *18*, 6292.

[29] D. Ren, L. Ahtapodov, J. S. Nilsen, J. Yang, A. Gustafsson, J. Huh, G. J. Conibeer, A. T. J. Van Helvoort, B.-O. Fimland, H. Weman, *Nano Lett.* **2018**, *18*, 2304.

[30] F. Zhang, X. Zhang, Z. Li, R. Yi, Z. Li, N. Wang, X. Xu, Z. Azimi, L. Li, M. Lysevych, X. Gan, Y. Lu, H. H. Tan, C. Jagadish, L. Fu, *Adv. Funct. Mater.* **2022**, *32*, 2103057.

[31] X. Zhang, R. Yi, N. Gagrani, Z. Li, F. Zhang, X. Gan, X. Yao, X. Yuan, N. Wang, J. Zhao, P. Chen, W. Lu, L. Fu, H. H. Tan, C. Jagadish, *ACS Nano* **2021**, *15*, 9126.

[32] Z. Azimi, N. Gagrani, J. Qu, O. L. C. Lem, S. Mokkapati, J. M. Cairney, R. Zheng, H. H. Tan, C. Jagadish, J. Wong-Leung, *Nanoscale Horiz.* **2021**, *6*, 559.

[33] J. A. Alanis, M. Lysevych, T. Burgess, D. Saxena, S. Mokkapati, S. Skalsky, X. Tang, P. Mitchell, A. S. Walton, H. H. Tan, C. Jagadish, P. Parkinson, *Nano Lett.* **2019**, *19*, 362.

[34] J. A. Alanis, Q. Chen, M. Lysevych, T. Burgess, L.i Li, Z. Liu, H. H. Tan, C. Jagadish, P. Parkinson, *Nanoscale Adv.* **2019**, *1*, 4393.

[35] M. O. Hill, P. Schmiedeke, C. Huang, S. Maddali, X. Hu, S. O. Hruszkewycz, J. J. Finley, G. Koblmüller, L. J. Lauhon, *ACS Nano* **2022**, *16*, 20281.

[36] J. A. Alanis, D. Saxena, S. Mokkapati, N. Jiang, K. Peng, X. Tang, L. Fu, H. H. Tan, C. Jagadish, P. Parkinson, *Nano Lett.* **2017**, *17*, 4860.

[37] T. Burgess, D. Saxena, S. Mokkapati, Z. Li, C. R. Hall, J. A. Davis, Y. Wang, L. M. Smith, L. Fu, P. Caroff, H. H. Tan, C. Jagadish, *Nat. Commun.* **2016**, *7*, 11927.

[38] K. H. Li, X. Liu, Q. Wang, S. Zhao, Z. Mi, *Nat. Nanotechnol.* **2015**, *10*, 140.

[39] D. Fekete, *Appl. Phys. Lett.* **2005**, *86*, 061115 .

[40] S. T. Yen, C.-P. Lee, *IEEE J. Quantum Electron.* **1998**, *34*, 1644.

[41] S. M. Shank, J. A. Varriano, G. W. Wicks, *Appl. Phys. Lett.* **1992**, *61*, 2851.

[42] K. J. Vahala, C. E. Zah, *Appl. Phys. Lett.* **1988**, *52*, 1945.

[43] J. C. Norman, D. Jung, Z. Zhang, Y. Wan, S. Liu, C. Shang, R. W. Herrick, W. W. Chow, A. C. Gossard, J. E. Bowers, *IEEE J. Quantum Electron.* **2019**, *55*, 2000511.

[44] D. G. Deppe, K. C. Hsieh, N. Holonyak, R. D. Burnham, R. L. Thornton, *J. Appl. Phys.* **1985**, *58*, 4515.

[45] M. J. Tambe, S. Ren, S. Gradecak, *Nano Lett.* **2010**, *10*, 4584.

[46] J. Qu, W. Choi, P. Katal Mohseni, X. Li, Y. Zhang, H. Chen, S. Ringer, R. Zheng, *ACS Appl. Mater. Interfaces* **2016**, *8*, 26244.

[47] G. P. S. Balasubramanian, E. Lebedkina, N. I. Goktas, J. B. Wagner, O. Hansen, R. Lapierre, E. Semenova, K. Mølhave, M. Beleggia, E. M. Fiordaliso, *Nanotechnology* **2022**, *33*, 475705.

[48] L. Pavesi, N. H. Ky, J. D. Ganière, F. K. Reinhart, N. Baba-Ali, I. Harrison, B. Tuck, M. Henini, *J. Appl. Phys.* **1992**, *71*, 2225.

[49] J. E. Stehr, M. Jansson, R. La, C. W. Tu, W. M. Chen, I. A. Buyanova, *Nano Express* **2020**, *1*, 020022.

[50] Y. G. Chai, R. Chow, C. E. C. Wood, *Appl. Phys. Lett.* **1981**, *39*, 800.

[51] J. E. Northrup, S. B. Zhang, *Phys. Rev. B* **1993**, *47*, 6791.

[52] T. Laine, K. Saarinen, J. Mäkinen, P. Hautojärvi, C. Corbel, L. N. Pfeiffer, P. H. Citrin, *Phys. Rev. B* **1996**, *54*, R11050.

[53] V. G. Dubrovskii, H. Hijazi, N. I. Goktas, R. R. Lapierre, *J. Phys. Chem. C* **2020**, *124*, 17299.

[54] M. Hilse, M. Ramsteiner, S. Breuer, L. Geelhaar, H. Riechert, *Appl. Phys. Lett.* **2010**, *96*, 193104.

[55] J. Dufouleur, C. Colombo, T. Garma, B. Ketterer, E. Uccelli, M. Nicotra, A. Fontcuberta I Morral, *Nano Lett.* **2010**, *10*, 1734.

[56] K. Tomioka, J. Motohisa, S. Hara, K. Hiruma, T. Fukui, *Nano Lett.* **2010**, *10*, 1639.

[57] S. Arab, M. Yao, C. Zhou, P. Daniel Dapkus, S. B. Cronin, *Appl. Phys. Lett.* **2016**, *108*, 182106.

[58] D. Ruhstorfer, S. Mejia, M. Ramsteiner, M. Döblinger, H. Riedl, J. J. Finley, G. Koblmüller, *Appl. Phys. Lett.* **2020**, *116*, 052101.

[59] D. Ruhstorfer, M. Döblinger, H. Riedl, J. J. Finley, G. Koblmüller, *J. Appl. Phys.* **2022**, *132*, 204302.

[60] A. Ajay, H. Jeong, T. Schreitmüller, M. Döblinger, D. Ruhstorfer, N. Mukhundhan, P. A. L. M. Koolen, J. J. Finley, G. Koblmüller, *Appl. Phys. Lett.* **2022**, *121*, 072107.

[61] H. W. Jeong, A. Ajay, H. Yu, M. Döblinger, N. Mukhundhan, J. J. Finley, G. Koblmüller, *Small* **2023**, *19*, 2207531.

[62] J. Becker, M. O. Hill, M. Sonner, J. Treu, M. Döblinger, A. Hirler, H. Riedl, J. J. Finley, L. Lauhon, G. Koblmüller, *ACS Nano* **2018**, *12*, 1603.

[63] M. Yao, C. Sheng, M. Ge, C.-Y. Chi, S. Cong, A. Nakano, P. D. Dapkus, C. Zhou, *ACS Nano* **2016**, *10*, 2424.

[64] K. Ikejiri, T. Sato, H. Yoshida, K. Hiruma, J. Motohisa, S. Hara, T. Fukui, *Nanotechnology* **2008**, *19*, 265604.

[65] C. Mead, C. Huang, N. Isik Goktas, E. M. Fiordaliso, R. R. Lapierre, L. J. Lauhon, *Nanotechnology* **2023**, *34*, 385701.

[66] M. Hilse, M. Ramsteiner, S. Breuer, L. Geelhaar, H. Riechert, *Appl. Phys. Lett.* **2004**, *96*, 193104 (2010).

[67] E. Dimakis, M. Ramsteiner, C.-N. Huang, A. Trampert, A. Davydok, A. Biermanns, U. Pietsch, H. Riechert, L. Geelhaar, *Appl. Phys. Lett.* **2013**, *103*, 143121.

[68] R. Murray, R. C. Newman, M. J. L. Sangster, R. B. Beall, J. J. Harris, P. J. Wright, J. Wagner, M. Ramsteiner, *J. Appl. Phys.* **1989**, *66*, 2589.

[69] J. Wagner, *Appl. Surf. Sci.* **1991**, *50*, 79.

[70] Y. G. Chai, R. Chow, C. E. C. Wood, *Appl. Phys. Lett.* **1981**, *39*, 800.

[71] M. J. Ashwin, R. C. Newman, K. Muraki, *J. Appl. Phys.* **1997**, *82*, 137.

[72] W. Walukiewicz, *Phys. Rev. B* **1990**, *41*, 10218.

[73] M. M. Sonner, M. Gnedel, J. C. Berlin, D. Rudolph, G. Koblmüller, H. J. Krenner, *Nanotechnology* **2021**, *32*, 505209.

[74] J. Toivonen, T. Hakkarainen, M. Sopanen, H. Lipsanen, J. Oila, K. Saarinen, *Appl. Phys. Lett.* **2003**, *82*, 40.

[75] R. A. Abram, G. N. Childs, P. A. Saunderson, *J. Phys. C: Solid State Phys.* **1984**, *17*, 6105.

[76] K.-S. Kim, D.-P. Han, H.-S. Kim, J.-I. Shim, *Appl. Phys. Lett.* **2014**, *104*, 091110.

[77] D. Rudolph, L. Schweickert, S. Morkötter, L. Hanschke, S. Hertenberger, M. Bichler, G. Koblmüller, G. Abstreiter, J. J. Finley, *New J. Phys.* **2013**, *15*, 113032.

[78] S. Perera, M. A. Fickenscher, H. E. Jackson, L. M. Smith, J. M. Yarrison-Rice, H. J. Joyce, Q. Gao, H. H. Tan, C. Jagadish, X. Zhang, J. Zou, *Appl. Phys. Lett.* **2008**, *93*, 053110.

[79] S. Watanabe, N. Yamada, M. Nagashima, Y. Ueki, C. Sasaki, Y. Yamada, T. Taguchi, K. Tadatomo, H. Okagawa, H. Kudo, *Appl. Phys. Lett.* **2003**, *83*, 4906.

[80] Y. Arakawa, H. Sakaki, *Appl. Phys. Lett.* **1982**, *4*, 939.

[81] J. Tatebayashi, S. Kako, J. Ho, Y. Ota, S. Iwamoto, Y. Arakawa, *Nat. Photonics* **2015**, *9*, 501.

[82] M. Zapf, C. Ronning, R. Röder, *Appl. Phys. Lett.* **2017**, *110*, 173103.

[83] N. K. Dutta, R. J. Nelson, *J. Appl. Phys.* **1982**, *53*, 74.

[84] S. Fathpour, Z. Mi, P. Bhattacharya, A. R. Kovsh, S. S. Mikhrin, I. L. Krestnikov, A. V. Kozhukhov, N. N. Ledentsov, *Appl. Phys. Lett.* **2004**, *85*, 5164.

[85] I. P. Marko, N. F. Massé, S. J. Sweeney, A. D. Andreev, A. R. Adams, N. Hatori, M. Sugawara, *Appl. Phys. Lett.* **2005**, *87*, 211114.

[86] I. C. Sandall, P. M. Smowton, J. D. Thomson, T. Badcock, D. J. Mowbray, H.-Y. Liu, M. Hopkinson, *Appl. Phys. Lett.* **2006**, *89*, 151118.

[87] F. Fischer, D. Schuh, M. Bichler, G. Abstreiter, M. Grayson, K. Neumaier, *Appl. Phys. Lett.* **2005**, *86*, 192106.

[88] S. Morkötter, N. Jeon, D. Rudolph, B. Loitsch, D. Spirkoska, E. Hoffmann, M. Döblinger, S. Matich, J. J. Finley, L. J. Lauhon, G. Abstreiter, G. Koblmüller, *Nano Lett.* **2015**, *15*, 3295.

[89] A. Thurn, J. Bissinger, S. Meinecke, P. Schmiedeke, S. S. Oh, W. W. Chow, K. Lüdge, G. Koblmüller, J. J. Finley, *Phys. Rev. Appl.* **2023**, *20*, 034045.